Convergence and Technologies

Cancer Research

Targeting the Temporal Dynamics of Hypoxia-Induced Tumor-Secreted Factors Halts Tumor Migration

Manjulata Singh[1], Xiao-Jun Tian[2,3], Vera S. Donnenberg[1,4], Alan M. Watson[5], JingYu Zhang[2], Laura P. Stabile[6], Simon C. Watkins[7], Jianhua Xing[2,8], and Shilpa Sant[1,8,9]

Abstract

Targeting microenvironmental factors that foster migratory cell phenotypes is a promising strategy for halting tumor migration. However, lack of mechanistic understanding of the emergence of migratory phenotypes impedes pharmaceutical drug development. Using our three-dimensional microtumor model with tight control over tumor size, we recapitulated the tumor size–induced hypoxic microenvironment and emergence of migratory phenotypes in microtumors from epithelial breast cells and patient-derived primary metastatic breast cancer cells, mesothelioma cells, and lung cancer xenograft cells. The microtumor models from various patient-derived tumor cells and patient-derived xenograft cells revealed upregulation of tumor-secreted factors, including matrix metalloproteinase-9 (MMP9), fibronectin (FN), and soluble E-cadherin, consistent with clinically reported elevated levels of FN and MMP9 in patient breast tumors compared with healthy mammary glands. Secreted factors in the conditioned media of large microtumors induced a migratory phenotype in nonhypoxic, nonmigratory small microtumors. Subsequent mathematical analyses identified a two-stage microtumor progression and migration mechanism whereby hypoxia induces a migratory phenotype in the initialization stage, which then becomes self-sustained through a positive feedback loop established among the tumor-secreted factors. Computational and experimental studies showed that inhibition of tumor-secreted factors effectively halts microtumor migration despite tumor-to-tumor variation in migration kinetics, while inhibition of hypoxia is effective only within a time window and is compromised by tumor-to-tumor variation, supporting our notion that hypoxia initiates migratory phenotypes but does not sustain it. In summary, we show that targeting temporal dynamics of evolving microenvironments, especially tumor-secreted factors during tumor progression, can halt tumor migration.

Significance: This study uses state-of-the-art three-dimensional microtumor models and computational approaches to highlight the temporal dynamics of tumor-secreted microenvironmental factors in inducing tumor migration.

Introduction

Metastases to distant organs are the major cause of mortality in patients with cancer (1, 2). For solid epithelial–stromal tumors, epithelial cells acquire a migratory phenotype, break away from the primary tumor, navigate through the extracellular matrix, and extravasate into the circulation to form secondary metastases (3, 4). Therefore, mechanistic understanding of the emergence of migratory phenotypes is important for identifying novel and effective treatment strategies to prevent metastases.

Tumor epithelial cells interact with the extracellular matrix and the neighboring tumor, stromal, and immune cells. They are exposed to various secreted factors presented in the local microenvironment, and they themselves shed/secrete various factors (secretome) to actively reshape the microenvironment, which in turn contribute to phenotypic plasticity and tumor progression (2, 5, 6). Hence, increasing number of emerging cancer treatments target secreted factors in tumor microenvironment (7–9). Unlike molecular therapies targeting the tumor cells, those targeting the microenvironments including tumor-secreted factors are expected to be less prone to adaptive changes in the tumor cells and thus, emergence of resistant cell populations (7). However, success of such therapies remains mixed. For example, hypoxia is known to contribute

[1]Department of Pharmaceutical Sciences, School of Pharmacy, University of Pittsburgh, Pittsburgh, Pennsylvania. [2]Department of Computational and Systems Biology, School of Medicine, University of Pittsburgh, Pittsburgh, Pennsylvania. [3]School of Biological and Health Systems Engineering, Arizona State University, Tempe, Arizona. [4]Department of Cardiothoracic Surgery, University of Pittsburgh School of Medicine, McGowan Institute for Regenerative Medicine, and UPMC-Hillman Cancer Center, University of Pittsburgh, Pittsburgh, Pennsylvania. [5]Center for Biologic Imaging, Center for Vaccine Research, and Department of Immunology, University of Pittsburgh, Pittsburgh, Pennsylvania. [6]Department of Pharmacology & Chemical Biology, UPMC-Hillman Cancer Center, Pittsburgh, Pennsylvania. [7]Center for Biologic Imaging and the Department of Cellular Biology, University of Pittsburgh, Pittsburgh, Pennsylvania. [8]UPMC-Hillman Cancer Center, University of Pittsburgh, Pittsburgh, Pennsylvania. [9]Department of Bioengineering, Swanson School of Engineering, and McGowan Institute for Regenerative Medicine, University of Pittsburgh, Pittsburgh, Pennsylvania.

Note: Supplementary data for this article are available at Cancer Research Online (http://cancerres.aacrjournals.org/).

M. Singh and X.-J. Tian contributed equally to this article.

Corresponding Authors: Shilpa Sant, University of Pittsburgh School of Pharmacy, 700 Technology Drive, PTC 4306, Pittsburgh, PA 15261. Phone: 412-648-9804; Fax: 412-624-1025; E-mail: shs149@pitt.edu; and Jianhua Xing, xing1@pitt.edu

Cancer Res 2019;79:2962–77

doi: 10.1158/0008-5472.CAN-18-3151

to hypoxic secretome (10) and activate several transcription factors (1) and epigenetic modifications (11). These can further induce cell phenotype changes such as conventional or partial epithelial-to-mesenchymal transition (EMT) that contributes to drug resistance and possibly, to tumor migration and metastasis (3, 11–17). However, hypoxia-targeted therapies combined with current standard-of-care therapies (e.g., chemotherapy or radiotherapy) showed mixed outcomes in several clinical trials (18–20). This failure is not so unexpected because tumor cells can maintain their aggressive behavior in nonhypoxic conditions after they extravasate away from the tumor mass, and thus, may not be affected by an antihypoxic therapy applied after tumor migration program is turned on. Therefore, an effective treatment strategy needs to tackle the intricate regulatory network that initiates, and maintains the tumor migratory phenotype (21).

Because hypoxia is one of the microenvironmental parameters implicated in inducing migratory phenotype and associated therapy resistance, it is important to have an experimental system that recapitulates spontaneously formed hypoxic microenvironment along with the tumor secretome. Traditional two-dimensional (2D) cell culture–based assays are unable to capture the constantly evolving dynamic *in vivo* microenvironment and are likely poor surrogates for studying emergence of migratory phenotypes (see recent review in ref. 13). Typical *in vitro* three-dimensional (3D) cultures such as spinner flasks (22–24) generate a broad size distribution of multicellular aggregates (microtumors), which present a technical difficulty for systematically studying the effect of tumor size–induced hypoxic microenvironment. To engineer controlled local microenvironment that is purely defined by microtumor size and tumor-secreted factors, we adopted microfabricated hydrogel microwells to generate hundreds of microtumors of uniform yet precisely controlled sizes from multiple cancer cell lines including breast, prostate and, head and neck cancer (24–28). Precise control over microtumor size translated in controlled hypoxic and metabolic microenvironments (25–28). By manipulating microtumor size alone and without any genetic manipulations or exogenous stimuli, we reproducibly generated two distinct phenotypes from the same noninvasive parent breast cancer cells: small nonhypoxic microtumors represent nonmigratory phenotype whereas large hypoxic microtumors exhibit migratory phenotype (25, 26, 28). Notably, the migratory cells in large microtumors could remember their phenotype and remain migratory even after dissociating into single-cell suspension and regrowing into small nonhypoxic microtumors (25). Therefore, our microtumor model recapitulates both, hypoxia-induced migratory phenotype in large microtumors and its subsequent maintenance under hypoxia-free microenvironment in small nonhypoxic microtumors.

The objective of this study was to investigate the mechanisms involved in the acquisition of migratory phenotype by the parent noninvasive breast cancer cells and its maintenance under hypoxia-free microenvironment using size-controlled microtumor models. We used only monocultures of tumor cells without other stromal cells to delineate how hypoxia-induced changes in the tumor-secreted factors generate migratory phenotypes in preinvasive parent cells. A tangible advantage of our microtumor platform is the ability to precisely and reproducibly study how the hypoxic microenvironment induces tumor migration in real time and in isolation from nontumor cells present *in vivo*, providing unique opportunity to define tumor-intrinsic mechanisms of transition from nonmigratory to migratory phenotype. We demonstrate a two-stage tumor progression mechanism that tumor size–induced hypoxia induces migratory phenotype in the initialization stage, which is subsequently maintained by feedback loop among tumor-secreted factors such as matrix metalloproteinases (MMP)/ soluble E-cadherin (sE-CAD)/ fibronectin (FN). We provide compelling evidence that targeting molecules involved in the maintenance stage, but not in the initialization axis of tumor progression, can be an effective treatment strategy that is less affected by tumor progression stage.

Materials and Methods

Chemicals and reagents

All chemicals and reagents were procured from Sigma-Aldrich unless specified. All antibodies were purchased from Santa Cruz Biotechnology except anti-vimentin (MA3-745), anti-β actin (MA5-15739) from Thermo Fisher Scientific; anti-ERK (9102S), and anti-pERK (4370P) from Cell Signaling Technology; anti-HIF1α (GTX127309) from GenTex and anti-fibronectin (610077) from BD Biosciences. GM6001 (MMP inhibitor) was procured from Millipore and Methyl 3-[[2-[4-(2-adamantyl) phenoxy] acetyl]amino]-4-hydroxybenzoate (HIF1α inhibitor) was obtained from Santa Cruz Biotechnology. Human E-Cadherin Quantikine ELISA Kit was purchased from R&D Systems.

Cell lines and cell culture

Breast cancer cell line T47D was purchased from ATCC and cell-culture supplies and media were obtained from Corning and Mediatech, respectively, unless specified. T47D cells were passaged and maintained in T75 flasks in DMEM (supplemented with 10% FBS; Hyclone) and 1% penicillin–streptomycin in 5% CO_2 at 37°C in a humidified incubator. Cell line authentication was done by University of Arizona Genetics Core by using PowerPlex16HS PCR Kit. Briefly, genomic DNA was genotyped for 15 Autosomal short-tandem repeat (STR) loci and Amelogenin using Promega Power Plex16HS PCR kit and the electropherogram were analyzed using Soft Genetics, Gene Marker Software Version 1.85. Alleles were matched to STR profile and a minimum of 80% match threshold was used for standardization of STR profiling and shared genetic history using ANSI database. Cells were maintained to attain 40%–60% confluence for further seeding into hydrogel microwell devices.

Primary cell cultures of malignant pleural effusions

Pleural effusions were collected from patients with metastatic breast cancer (mBC) or mesothelioma as waste materials during therapeutic drainage. Samples were anonymized by an honest broker and provided along with relevant clinical information, to the laboratory according to University of Pittsburgh IRB exemption (0503126, VSD). The cells were cryopreserved in 1.25 mL vials ($\sim 50 \times 10^6$ cells/vial) in MEM containing 10% DMSO and 20% calf serum. The cryopreserved cells were carefully thawed in ice cold DMEM supplemented with 50% calf serum, suspended in complete mammary epithelial growth medium (MEGM, catalog

no. CC-3151, Lonza) supplemented with 10% FBS (catalog no. SH30088.03, HyClone, GE Healthcare Life Sciences) and 10% autologous cell-free pleural fluid. Complete MEGM consists of Epithelial Cell Basal Medium supplemented with bovine pituitary extract (BPE, Lonza, catalog no. CC-4009G) human epidermal growth factor (rhEGF, 10 ng/mL, Lonza, catalog no. CC-4017G), hydrocortisone (0.5 μg/mL, Lonza, catalog no. CC-4031G), gentamicin sulfate plus amphotericin B (Lonza, catalog no. CC-4081G), and insulin (10 μg/mL, Lonza catalog no. CC-4021G). The cells were initially plated in 10-cm petri dishes at a culture density of 1–1.5 $\times$ 10^5 cells/cm^2, grown to semiconfluence, trypsinized, and split 1 to 3. All samples were analyzed at passage 0 and 1.

Multicolor flow cytometry on unpassaged metastatic breast cancer samples (MPE175)

Detailed methods used to disaggregate, stain, and analyze unpassaged metastatic breast cancer samples have been described in detail (29). Nonspecific binding of fluorochrome-conjugated antibodies was minimized by preincubating pelleted cell suspensions for 5 minutes with neat decomplemented (56°C, 30 minutes) mouse serum (5 μL; ref. 30). The cells were then pelleted again by centrifugation and residual fluid aspirated. All antibodies were added at a fixed volume (2 μL) representing an approximate dilution of 1:5. Cells were first stained for surface markers. The order of addition was as follows: CD326/EpCAM-APC (Miltenyi Biotec, catalog no. 130-098-118), CD45-APCCy7 (BD Biosciences, catalog no. 348805), CD44-PECy7 (Abcam, catalog no. ab46793), CD90-APC (BD Biosciences, catalog no. 559869), CD14-PECy5 (Beckman-Coulter, catalog no. IM2640U), CD33-PECy5 (Beckman-Coulter, catalog no. IM2647U), Glycophorin A-PECy5 (BD Biosciences, catalog no. 559944), and CD73-PE (BD Pharmingen, catalog no. 550257). Unbound antibodies were washed and cells were fixed with 2% methanol-free formaldehyde (Polysciences). Cells were then permeabilized with 0.1% Saponin (Beckman Coulter) in PBS with 0.5% human serum albumin (10 minutes at room temperature); cell pellets were incubated with 5 μL of neat mouse serum for 5 minutes, centrifuged, and decanted. The cell pellet was disaggregated and incubated with 2 μL of anti-pan cytokeratin (CTK, Abcam, catalog no. ab52460) and vimentin (VIM; BD Pharmingen catalog no. 562338) for 30 minutes. Cell pellets were diluted to a concentration of 10 $\times$ 10^6 cells/400 μL of staining buffer and DAPI (Life Technologies, catalog no. D1306) was added 10 minutes before sample acquisition, to a final concentration of 7.7 μg/mL and 40 μL/10^6 cells. In this application, DAPI was used as a DNA stain in fixed permeabilized cells because it permits removal of artifacts associated with tissue digestion and also provides information on cell DNA content. Stained cells were acquired on a Beckman Coulter Gallios cytometer calibrated to preestablished PMT target channels. Offline compensation and analyses were performed using VenturiOne Software (Applied Cytometry) as described previously (30). Spectral compensation matrices were calculated for each staining combination within each experiment using single-stained mouse IgG Capture Beads (Becton Dickinson, catalog no. 552843) for each tandem fluorochrome, and BD Calibrite beads for PE and APC controls (Becton Dickinson, catalog no. 340486).

3D culture and microtumor fabrication

Nonadhesive hydrogel microwell devices of 150 and 600 μm were microfabricated using polyethylene glycol dimethacrylate (PEGDMA, 1,000 Da) and polydimethyl siloxane (PDMS) molds as described previously (25, 26). PDMS molds with 150 and 600 μm posts (1:1 aspect ratio of height: diameter) were placed on PEGDMA solution (20% w/v) mixed with Photoinitiator (Irgacure-1959, 1% w/v, Ciba AG CH-4002) and photo-crosslinked using the OmniCure S2000 Curing Station (EXFO). Subsequently, T47D cell suspension in growth media (200 μL, 4.0 $\times$ 10^6 cells/device) was seeded on the 2 $\times$ 2 cm^2 hydrogel microwell device and cultured in a humidified 5% CO_2 incubator. Microtumors were cultured up to 6 days with replacement of 50% media with equal amount of fresh media every day and harvested on day 6 and processed further as required or frozen at −80°C. Methods for isolation of primary cells from primary mBC, mesothelioma and patient-derived mouse xenograft (PDX) as well as fabrication of 3D microtumors from these primary tumor cells and xenografts is described in Supplementary Information (Materials and Methods).

Clinical data for FN and MMP9 expression in patient tumors

For FN1 and matrix metalloprotease 9 (MMP9) expression profile analysis in patient tumors, we integrated high-quality metadata of human that were obtained by AffyU133Plus2 platform expression arrays from public repositories, such as GEO. 3735 Homo sapiens samples were included in the results. The original targeted gene expression profile in nine subcategories of cancers as well as normal tissue was extracted and normalized by Genevestigator.

Treatment of microtumors with conditioned media and various inhibitors

To study the effect of hypoxic secretome, 150 μm microtumors were treated with 50% conditioned media (CM) of 600 μm microtumors (denoted as "600/CM") from day 3 to day 6 every day. To investigate the role of sE-CAD on microtumor migration, 150 μm microtumors were treated with recombinant human E-CAD, Fc chimera protein (20 μg/mL, R&D Systems) for predetermined time.

Hypoxia-inducible factor 1 alpha (HIF1α) was inhibited chemically by treatment of 600 μm microtumors with growth media containing HIF1α inhibitor, methyl 3-[[2-[4-(2-adamantyl) phenoxy] acetyl] amino]-4-hydroxybenzoate (1.0 μmol/L) at different time points. MMP inhibition was achieved by treating 600 μm microtumors with broad spectrum MMP inhibitor (GM6001, 20 μmol/L). To scavenge sE-CAD secreted in the CM, 600 μm microtumors were treated every day with ectodomain antibody (H-108, 40 μg/mL, Santa Cruz Biotechnology) in the growth media from day 3 to day 6 or day 4 to day 6.

After CM and various inhibitor treatment studies, mRNA were isolated from control (untreated) and treated microtumors and EMT marker expression was determined by qRT-PCR. Similarly, protein expression was estimated by Western blotting analysis.

Kinetics of microtumor migration

The aggressive phenotype of microtumors was assessed by measuring the distance of migration (d) and extent of migration (%). The distance of migration (d) was estimated by measuring the average length of straight lines drawn perpendicular to periphery of the well up to the leading edge, covering the entire migratory

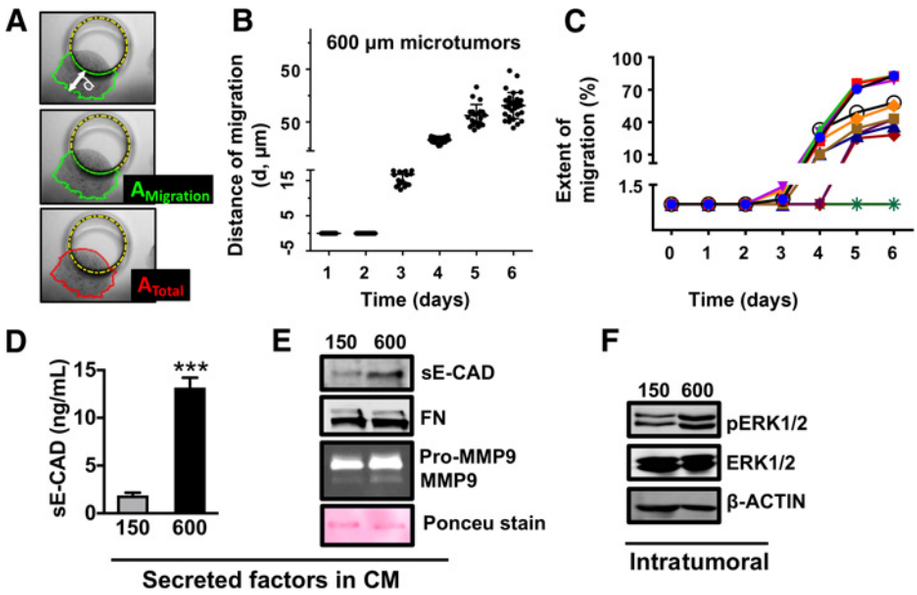

Figure 1.
Large microtumors exhibit hypoxia, collective migration, and aggressive phenotype. **A,** Schematic defining distance of migration (d), area of microtumor migrated out of the microwell ($A_{Migration}$), and total area of the microtumor (A_{Total}). **B,** Distance of migration for individual microtumors; each dot represents data for individual microtumor. **C,** Migration trajectories of individual 600 μm microtumors from days 1 to 6 showing intertumoral variation in migration kinetics; extent of migration for each time point was calculated as migrated distance/the total area of microtumor × 100. Levels of sE-CAD (ELISA; **D**) and sE-CAD, FN, Pro-MMP9, and MMP9 (Western blot; **E**) in CM; pERK expression in microtumor cell lysates (**F**). Data presented are representative from three independent experiments ($n = 3$; ***, $P < 0.001$; unpaired t test).

front using ImageJ. Of note, distance of migration for each microtumor was average of approximately ≥10 such perpendicular lines and was represented as the distance in microns. The extent of migration is the percentage of the area of the microtumor that is migrated out of the microwells ($A_{Migration}$) normalized with the total area of the microtumor (A_{Total}), [extent = $A_{Migration}/A_{Total}$ *100]; (see Fig. 1A) and was measured by ImageJ using analyze > set scale> Ctrl+T> measure tools.

Protein extraction and Western blot analysis

Frozen microtumor samples were lysed in radioimmunoprecipitation assay (RIPA) buffer containing Tris (50 mmol/L, pH 7.4), sodium chloride (150 mmol/L), sodium deoxycholate (0.5%), NP-40 (1%), phenylmethane sulfonyl fluoride (0.05 mmol/L), and protease inhibitor cocktail for mammalian tissue extract and phosphatase inhibitor (Sigma-Aldrich). Proteins secreted in the CM (sE-CAD and FN) were measured by resolving 50 μL of CM on 8%–10% polyacrylamide gel, transferring them to polyvinylidene difluoride membrane and probing them with respective antibodies. Of note, CM of 150 and 600 μm microtumors were collected from the hydrogel microwell devices that have same number of cells. To match the cell number of 150 and 600 μm microwell devices, cells/microtumor were calculated for both 150 and 600 μm microtumors. Subsequently, the dimensions of each device were adjusted to contain number of microtumors totaling to the same total cell number/device. Western blot analysis was performed for primary antibodies against vimentin (1:1,000), fibronectin (1:1,000), E-CAD (1:1,000), pERK (1:1,000), ERK (1:1,000), and β-actin (1:2,000) as described previously (25). Membranes were scanned by Odyssey Infrared Imaging System (LI-COR Biosciences) and colored images were converted to grayscale images by using Odyssey 3.0 software. Quantification of blots was done by ImageJ Software (NIH, USA) and normalization of densitometry was done by comparing with β-actin. The data are expressed as fold change compared with control/600 ($n = 3$).

Measurement of shed sE-CAD in the CM by ELISA

sE-CAD levels in the CM of 150 and 600 μm microtumors and inhibition studies were measured by quantitative ELISA (R&D Systems, DCADE0) according to the manufacturer's protocol. Of note, CM of 150 and 600 μm microtumors were collected from the hydrogel microwell devices that have same number of cells as mentioned above for Western blotting. All the CM were diluted (1:2) using dilution buffer from the kit before assay as described in the instruction manual. The standards and samples (50 μL) were pipetted into the E-CAD antibody precoated wells of microplate and incubated for 2 hours at room temperature on rocking platform. Any unbound material was removed by four times washing with wash buffer, an enzyme-linked polyclonal antibody specific for E-CAD was added to the wells and incubated for 2 hours at room temperature on rocker. Any unbound antibody-enzyme reagent was washed with wash buffer, followed by addition of a substrate solution and incubation for 30 minutes to develop the color. The reaction was stopped using stop solution and absorbance was measured at 450 nm. Each sample was measured in duplicate. The concentrations of sE-CAD were determined by extrapolating the values on the standard curve followed by multiplication of dilution factor and represented as ng/mL.

Immunostaining and confocal microscopy

E-Cadherin-GFP–expressing microtumors were cleared using CUBIC R1 (31). The clearing solution was removed by washing with CUBIC IHC buffer (PBS; 0.1% Triton X-100; 0.5% BSA; 0.01% Sodium Azide) and then stained with anti-vimentin (Abcam, ab73159) for 24 hours. Samples were then washed and incubated with anti–chicken-Cy5 for 24 hours (Jackson ImmunoResearch, 703-175-155). Samples were washed again and placed in CUBIC R2 without triethanolamine (32) containing Hoechst for 24 hours prior to imaging. All incubation steps were done at 37°C with gentle movement. The immunostaining

protocol was optimized to ensure antibody penetration throughout the volume of microtumors. Volumes were acquired over whole microtumors using a Nikon Ti-E equipped with a Bruker SFC and excitation at 405, 488, and 640 nm. The Voxel size was $0.4 \times 0.4 \times 5.0$ μm using an Apo 40x WI λS DIC N2 objective. Images were prepared in NIS Elements v4.51.00. Preparation of publication quality images included rolling ball background correction and local contrast enhancement.

RNA isolation and qRT-PCR analysis

RNA was isolated from all the samples by using GeneJET RNA Purification Kit (Thermo Fisher Scientific) as per the manufacturer's protocol. RNA quantity was measured by absorbance ratio at 260/280 nm and integrity was verified on 1% agarose gel. The mRNA expression of EMT markers such as VIM, FN, E-CAD, and MMP9 was analyzed by qRT-PCR using iTaq Universal SYBR Green One-Step RT-PCR Kit (BioRad Laboratories) and 7500 Fast Real-Time PCR System (Applied Biosystems) using β-Actin as control house-keeping gene. The mRNA expression was quantified using the $2^{-\Delta\Delta C_t}$ and presented as the mean ± SEM as fold change compared with controls (150 or 600 μm microtumors). Primer sequences are given in Supplementary Table S1.

Gelatin zymography

MMPs are responsible for cleavage of ectodomain E-CAD to generate 80 kDa sE-CAD. To estimate the levels of MMPs in the CM, gelatin zymography was performed as described by Frankowski and colleagues (33). Briefly, 50 μL of CM was mixed with nonreducing sample buffer and separated on 7% polyacrylamide gel containing 1.0% porcine gelatin Type A (Sigma). Gel was washed three times using wash buffer containing 25% v/v Triton X-100. Subsequently, the gel was incubated in developing buffer containing 50 mmol/L Tris, 10 mmol/L $CaCl_2$ and 0.02% sodium azide, for 48 hours at 37°C. Staining was done for 40 minutes using Coomassie Blue staining solution and destaining was done until the bands appeared. Imaging was done using GelDoc (BioRad) and quantification was done by densitometric analysis of bands by ImageJ.

Statistical analysis

Statistical analysis was done using GraphPad Prism7. All the values were presented as mean ± SEM. Unpaired *t* test was used to compare the significance between two groups. For multiple comparisons (effects of inhibitor treatments), data were analyzed by one-way ANOVA, followed by a Tukey test. A *P* value less than 0.05 was considered significant.

Mathematical modeling and analysis

A set of ordinary differential equations (ODE) to model the N-terminal E-cadherin shedding is applied in the theoretical analysis (details can be found in the Supplementary Material). The model quantitatively captures the dynamics of the core regulatory network that governs the N-terminal E-cadherin shedding in hypoxic microenvironment. The default state is the nonmigratory phenotype, in which the levels of the HIF1α, MMPs, and sE-CAD are low. The quantitative model consisted of 4 ODEs with 20 kinetic rate parameters (Supplementary Table S2). The bifurcation analysis was performed with the software Oscill8 (http://oscill8.sourceforge.net/). For HIF1α inhibition simulation, the HIF1α–mediated expression rate of MMPs is set to 1/10 of its original value while for the sE-CAD inhibition, the sE-CAD–mediated expression rate of ERK is set to 1/10 of its original value. For the MMP inhibition, the shedding rate of sE-CAD mediated by MMPs is set to 1/10 of its original value. All the concentrations are in a reduced unit. More detail is provided in Supplementary Information (Materials and Methods).

Results

Large microtumors exhibit hypoxia, collective migration, and aggressive phenotype

We adopted our microfabricated hydrogel microwell platform (25, 26) to generate uniform size T47D microtumors of 100–120 μm (referred as "small" microtumors) and 500–600 μm in diameter (referred as "large" microtumors). We selected 150 and 600 μm microwells to engineer nonhypoxic and hypoxic microenvironments based on our previous studies (25, 26, 28) as well as clinically reported tumor lesion sizes (34).

We cultured small and large size-controlled microtumors of noninvasive human T47D cells in microwell arrays for 6 days. While small microtumors remained nonmigratory after 6 days in culture, large microtumors moved toward the wall of the microwells and showed collective migration out of the wells (Supplementary Fig. S1Ai and S1Aii; Supplementary Video) starting from day 3. Both small and large microtumors exhibited similar rate of proliferation (about 1.5–2 fold; ref. 28), ruling out the differences in proliferation or cell crowding in the microwell as the cause of migration. We quantified the distance of migration (d), area of the migrated portion ($A_{Migration}$), and total microtumor area (A_{Total}) using ImageJ (Fig. 1A). Despite highly homogeneous size distribution on the same 2×2 cm^2 device, we observed microtumor-to-microtumor variation in the migration kinetics of large microtumors, parallel to the well-documented cell-to-cell variation (35). We quantified observed variations in migration kinetics of individual microtumors by the migrated distance (d) and the extent of migration ($A_{Migration}/A_{Total}{}^{*}100$; Fig. 1B and C; Supplementary Fig. S1B). We conjectured that the different behaviors of 150 and 600 μm microtumors result from size-associated changes in their microenvironments. Therefore, we measured intratumoral expression of HIF1α, EMT markers (VIM and FN), and levels of tumor-secreted factors including MMPs, FN, and sE-CAD in the CM. We observed upregulation of HIF1α protein in cell lysates (Supplementary Fig. S1C) and upregulation of mesenchymal markers, VIM and FN, without loss of epithelial marker, E-CAD (Supplementary Fig. S1D), suggesting that the migratory behavior of large microtumors represents "cohesive or collective migration" that requires E-CAD (4, 36). Indeed, immunostaining of large T47D microtumors showed presence of $E\text{-}CAD^{+}/VIM^{+}$ cells at the periphery without loss of E-CAD (Supplementary Fig. S1E, white arrows). Large microtumor CM showed increased levels of sE-CAD (Fig. 1D and E), FN, Pro-MMP9, and MMP9 compared with the small ones (Fig. 1E). The downstream ERK was activated as shown by upregulation of pERK in large microtumors (Fig. 1F). These results indicate that large tumor size induces hypoxic tumor microenvironments, higher levels of tumor-secreted factors (sE-CAD, FN, MMP9) and collective migration possibly due to the acquisition of mesenchymal features without loss of E-CAD. Interestingly,

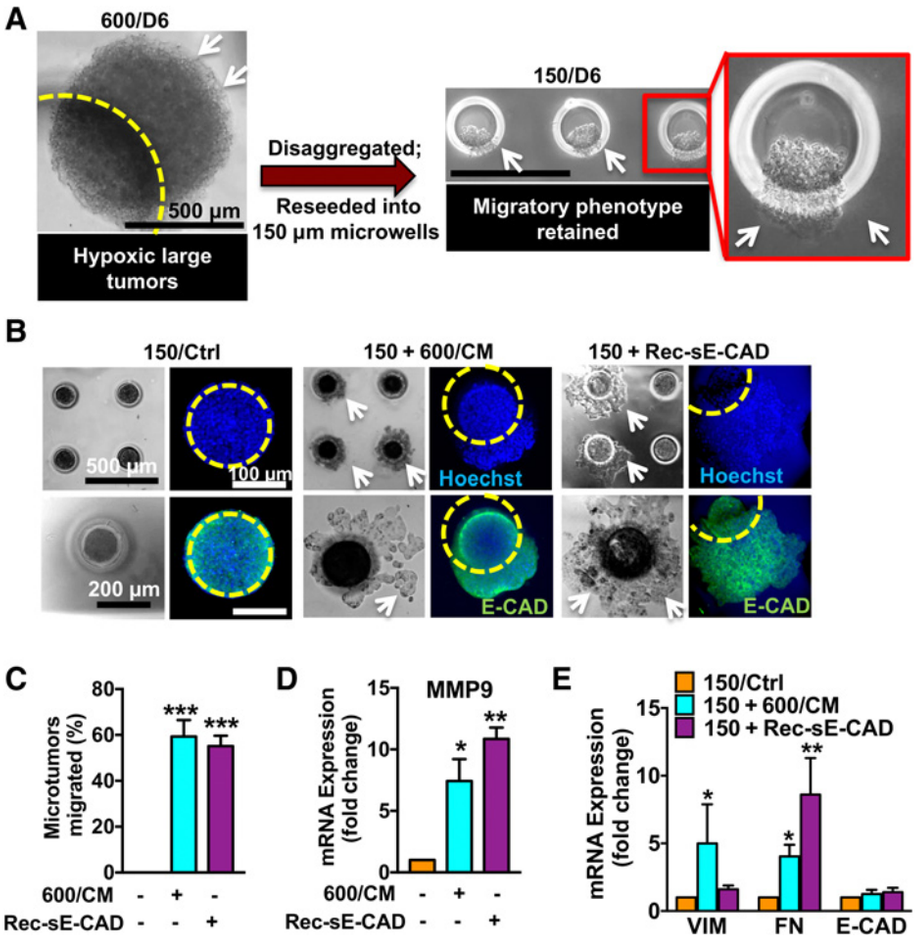

Figure 2.

Recombinant sE-CAD and hypoxic secretome (CM) induce collective migration in nonmigratory 150 μm microtumors. **A,** The 600 μm microtumors maintained their migratory phenotype (white arrows) even after disrupting hypoxia (disaggregation) and regrowing them into nonhypoxic 150 μm microtumors (inset). **B,** Representative images showing collective migration (white arrows) in 600/CM and Rec-sE-CAD–treated 150 μm microtumors without loss of E-CAD (green). Blue, cell nuclei; yellow circle, boundary of a microwell. **C** and **D,** Effect of 600/CM and Rec-sE-CAD treatments on migration (**C**) and mRNA expression (**D**) of MMP9 and VIM, FN, and E-CAD in treated 150 μm microtumors (**E**). Data are presented as mean ± SD (**C**) and mean ± SEM (**D** and **E**) from three independent experiments. *, $P < 0.05$; **, $P < 0.01$; ***, $P < 0.001$ with respect to untreated 150 μm microtumors.

we observed intratumoral differences in E-CAD and VIM expression along with intertumoral differences in migration kinetics in large microtumors.

Hypoxic tumor CM contain factors that can induce collective migration in nonhypoxic, nonmigratory small microtumors

Next, we asked whether hypoxia alone is responsible for inducing the migratory phenotype in large microtumors. In our previous work, HIF1α knockdown in large microtumors either by siRNA or pharmacologic inhibition from day 1 downregulated expression of mesenchymal markers and suppressed migration in large microtumors (25), suggesting possible role of hypoxic preconditioning and HIF1α stabilization in migration as suggested by others (37, 38). When nonhypoxic small microtumors were dissociated into single cells and regrown into large ones, they acquired migratory phenotype, confirming the role of hypoxic microenvironment in migration (25). Interestingly, when large microtumors were dissociated into single cells to remove the hypoxic microenvironment and regrown into small microtumors, they sustained their migratory phenotype (Fig. 2A). This suggests that the hypoxia-induced migratory phenotype is not reversible even after removal of hypoxic microenvironment. Our observation that environmental preconditioning (such as hypoxia) may predispose to aggressive tumor progression is consistent with previous studies showing that tail vein injection of tumor cells exposed to hypoxic conditions, followed by reoxygenation, resulted in increased metastasis (16, 17). We hypothesized that the hypoxic CM of large microtumors (600/CM) contain factors that contribute to maintain the migratory phenotype. When treated with 50% 600/CM every day from days 3 to 6, 60% of otherwise nonhypoxic, nonmigratory small microtumors became migratory (Fig. 2B and C).

The 600/CM contain multiple factors. Although we did not perform full secretome analysis, 600/CM showed elevated levels of sE-CAD compared with the 150/CM (Fig. 1D and E). Treatment with recombinant human sE-CAD (Rec-sE-CAD) also induced migration in more than 60% small microtumors (Fig. 2B and C). Both, 600/CM and Rec-sE-CAD treatments induced collective migration without loss of E-CAD (green, Fig. 2B). sE-CAD is known to upregulate MMP expression (39). Indeed, both 600/CM- and Rec-sE-CAD–treated 150 μm microtumors showed more than 8-fold increase in MMP9 expression (Fig. 2D). 600/CM–treated small microtumors showed significantly upregulated FN (4.0 ± 0.9 fold) and VIM (5.0 ± 2.9 fold), while those treated with Rec-sE-CAD significantly upregulated only FN (8.6 ± 2.7 folds) with no effect on VIM (Fig. 2E). These results confirmed that either 600/CM or sE-CAD alone could induce the migratory phenotype in nonmigratory (150 μm) epithelial microtumors albeit they have differential effects on regulating VIM expression. In

comparison, 150/CM did not affect migratory behavior of either small or large microtumors (Supplementary Fig. S2A and S2B). While our data demonstrate the role of 600/CM in inducing migratory phenotype in nonmigratory small microtumors, other possible mechanisms such as epigenetics may also contribute to the emergence and maintenance of the migratory phenotype.

Patient tumors, as well as microtumors of primary patient-derived tumor cells and PDX cells, show upregulation of FN, MMP9, and sE-CAD in their secretome

To investigate the clinical relevance of FN and MMP9, we extracted clinical data from various breast cancer types from a set of 3,735 human samples by Genevestigator and analyzed them with AffyU133Plus2. Expression of FN and MMP9 was higher in

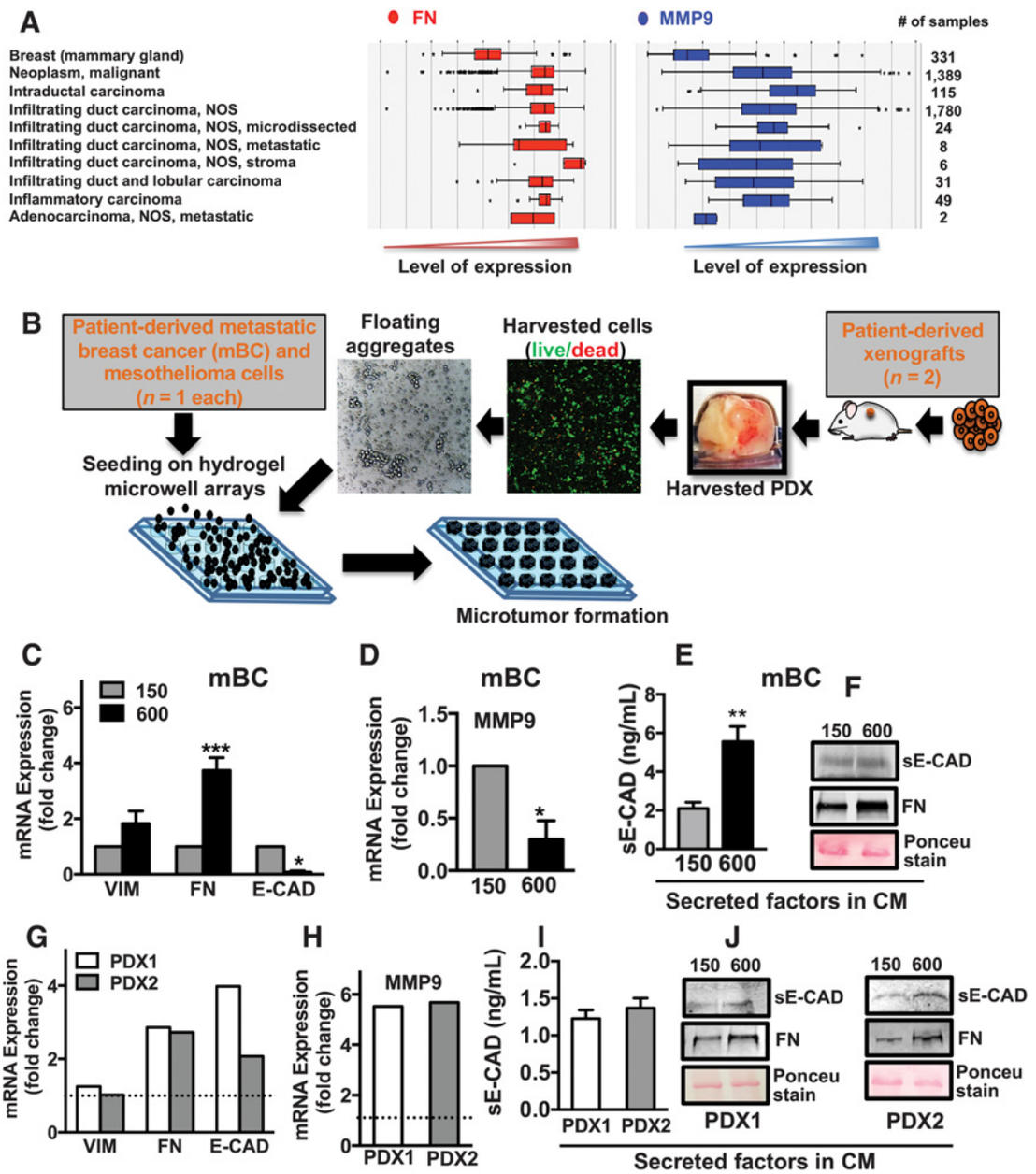

Figure 3.

Tumor secretome in patient tumors, microtumors of primary tumors, and PDX cells showed upregulation of FN, MMP9, and sE-CAD. **A,** Analysis of clinical dataset showed higher levels of FN and MMP9 in breast carcinomas compared with normal mammary gland. **B,** Hydrogel microwell arrays (150 and 600 μm) were used to generate the microtumors from patient-derived primary mBC cells (one patient), mesothelioma cells (one patient), and non–small cell lung cancer PDX model (two PDX tumors). Analysis of mRNA expression of VIM, FN, E-CAD (**C**), and MMP9 (**D**); protein levels of sE-CAD (**E** and **F**) and FN (**F**) in the mBC cell–derived microtumors and, similarly, in the PDX cell–derived microtumors (**G–J**). Dotted line in **G** and **H** refers to expression in small microtumors; nondetectable sE-CAD levels in small microtumors (**I**). *, $P < 0.05$; **, $P < 0.01$; ***, $P < 0.001$, unpaired *t* test.

various breast carcinomas compared with the normal mammary gland (Fig. 3A). Furthermore, we fabricated small and large microtumors using primary cancer cells derived from fresh mBC (1 patient sample), mesothelioma (1 patient sample), and lung PDX-derived cells (2 patient samples; Fig. 3B). Representative photomicrographs of malignant pleural effusions used in this study are shown in Supplementary Figs. S3 and S4. Despite the metastatic and highly invasive nature of malignant pleural effusions, morphologic characterization of mBC cells revealed microtumor clusters (Supplementary Fig. S3A). Flow-sorted aneuploidy tumor cells revealed mixed population of cytokeratin $(CTK)^+$/VIM^+ and only VIM^+ cells with small subpopulation of cells expressing surface mesenchymal markers (CD44, CD90; Supplementary Fig. S3B and S3C). Patient- and xenograft-derived primary cancer cells formed small and large microtumors in our microwell arrays, albeit, the microtumor sizes immediately after seeding were smaller than breast cancer cell line–derived microtumors (Supplementary Fig. S4A–S4C). This could be attributed to the differences in the cell size and compaction ability of individual cells isolated from different tumors. We have reported similar observations with head and neck cancer cell lines (25, 26). Notably, the microtumors of primary cancer cells from different tumor types also recapitulated the results obtained with the breast cancer cell lines, where large microtumors showed migratory phenotype on days 6–8 while smaller ones remained nonmigratory. Compared with the small microtumors, the large microtumors of patient-derived mBC cells showed 4-fold upregulation of FN with a slight but not significant change in *VIM* mRNA (Fig. 3C). Interestingly, we also observed significant downregulation of *E-CAD* and *MMP9* mRNA (Fig. 3C and D). This could be because the primary mBC cells are derived from highly metastatic pleural effusions and may have molecular subtype different than T47D cells. Despite the microtumor clusters present in mBC pleural effusions as shown here, the mesenchymal phenotype is predominant (30). We also observed increased levels of sE-CAD (5.56 ± 0.77 ng/mL) in large compared with small microtumors (2.1 ± 0.32 ng/mL) by ELISA (Fig. 3E). Western blots revealed increased levels of sE-CAD and FN in 600/CM compared with small nonmigratory mBC microtumors (Fig. 3F). Similarly, we observed significant upregulation of *FN* (2.5-fold) and *MMP9* (5-fold) in large compared with small microtumors of lung PDX (dotted line, Fig. 3G and H). ELISA and Western blots showed high levels of sE-CAD and FN in the CM of large PDX (Fig. 3I and J) and mesothelioma microtumors (Supplementary Fig. S4D and S4E). Small lung PDX microtumors had nondetectable levels of sE-CAD measured by ELISA. These results indicate that our microtumor model can be easily adapted to patient- and xenograft-derived primary cancer cells across multiple tumor types such as breast, mesothelioma, and lung tumors.

Mathematical model predicts a two-stage mechanism for microtumor progression and migration

On the basis of the above experimental findings and our previous study (25), we constructed a minimal regulatory network describing how microtumor migration is coupled to its microenvironment (Fig. 4A; Supplementary Fig. S5). Here, we focus on how the regulators including HIF1α, MMP9, sE-CAD, and FN control the migratory phenotype. Increase in microtumor size leads to hypoxia, which stabilizes HIF1α (37, 38). HIF1α can increase MMP9 expression (37), which can promote cleavage E-CAD to generate sE-CAD. Abnormally elevated levels of sE-CAD have been reported in various types of cancers (40, 41). sE-CAD can bind and activate the EGFR family (HER1-4), which further activates the ERK pathway (42–44) involved in the tumor cell proliferation. Moreover, pro-MMP9 and FN are targets of ERK1/2 (9, 44–46). For simplicity, these intermediate regulators (pro-MMP9, ERK1/2) are taken implicitly in our minimal model. This completes a positive feedback loop among the microtumor-secreted factors, MMP9, sE-CAD, and FN. We hypothesized that this positive feedback is critical for collective migration of microtumors. We built a mathematical model to describe the dynamics of these regulators with a set of ODEs as shown in Fig. 4B (see Supplementary Material for details).

Through bifurcation analysis, we found that within a broad parameter range, the mathematical model gives an irreversible bistable switch. The level of [sE-CAD] is low in the CM of small microtumors (Fig. 4C, point 1). With increase in the tumor size, [sE-CAD] initially increases very slowly until a threshold (Saddle-Node bifurcation point, SN) of the microtumor size is reached, above which, [sE-CAD] jumps to a higher value (Fig. 4C, point 2). Here, we used [sE-CAD] as a marker because it is experimentally straightforward to measure its levels and we have shown that the CM of migratory large microtumors contains higher [sE-CAD] than that of nonmigratory small microtumors (Fig. 1D and E). It should be noted that this bistable switch is irreversible because [sE-CAD] remains high even after large microtumors are dissociated and regrown as small ones (Fig. 4C, point 3), just as what we observed experimentally (Fig. 2A). The irreversibility of the switch is important for the collective migration because it implies that the cells in large microtumor can maintain their migratory phenotype even after escaping the hypoxic core or disaggregating from the tumor. This mathematical analysis suggests a two-stage tumor progression mechanism (Fig. 4A), where hypoxia is important in the early initiation stage of tumor progression, and components of the MMPs/sE-CAD/FN feedback loop work synergistically to maintain the migratory phenotype. Indeed, the modeling results in Fig. 4D predict that treatment with 600/CM (containing MMP9+sE-CAD, green line) or Rec-sE-CAD (blue line) shifts the threshold of microtumor size below 200 μm for [sE-CAD] and tumor migration propensity. This was confirmed by our experimental results where treatment with 600/CM or Rec-sE-CAD induced migration in otherwise nonmigratory 150 μm microtumors (Fig. 2B and C). It is noted that patient-derived mBC microtumors start to migrate before they reach 500–600 μm in diameter (Supplementary Fig. S4A). That is, the threshold size for migration of these metastatic microtumors is lower than that of T47D microtumors. This may be due to the differences in the cell/tumor subtype, baseline phenotype of the cells, etc.

Our modeling studies reveal that a microtumor with size exceeding the critical value (SN; Fig. 4C) generates and then maintains a microenvironment with high [sE-CAD] and starts to migrate. Because of stochasticity such as cell growth and division rates, the onset as well as the kinetics of individual microtumor migration may vary, which we refer to as "dynamic intertumoral variation." Figure 4E shows simulated temporal dynamics of increase in [sE-CAD] in the CM of individual 150 and 600 μm microtumors, where the dynamic intertumoral variation manifests itself, especially for the 600 μm microtumors. Consequently, individual microtumors start to migrate at different times after day 2 (Fig. 4F), and within a range of microtumor sizes, our mathematical model predicts mixtures of migratory and nonmigratory microtumors as we observed experimentally for T47D

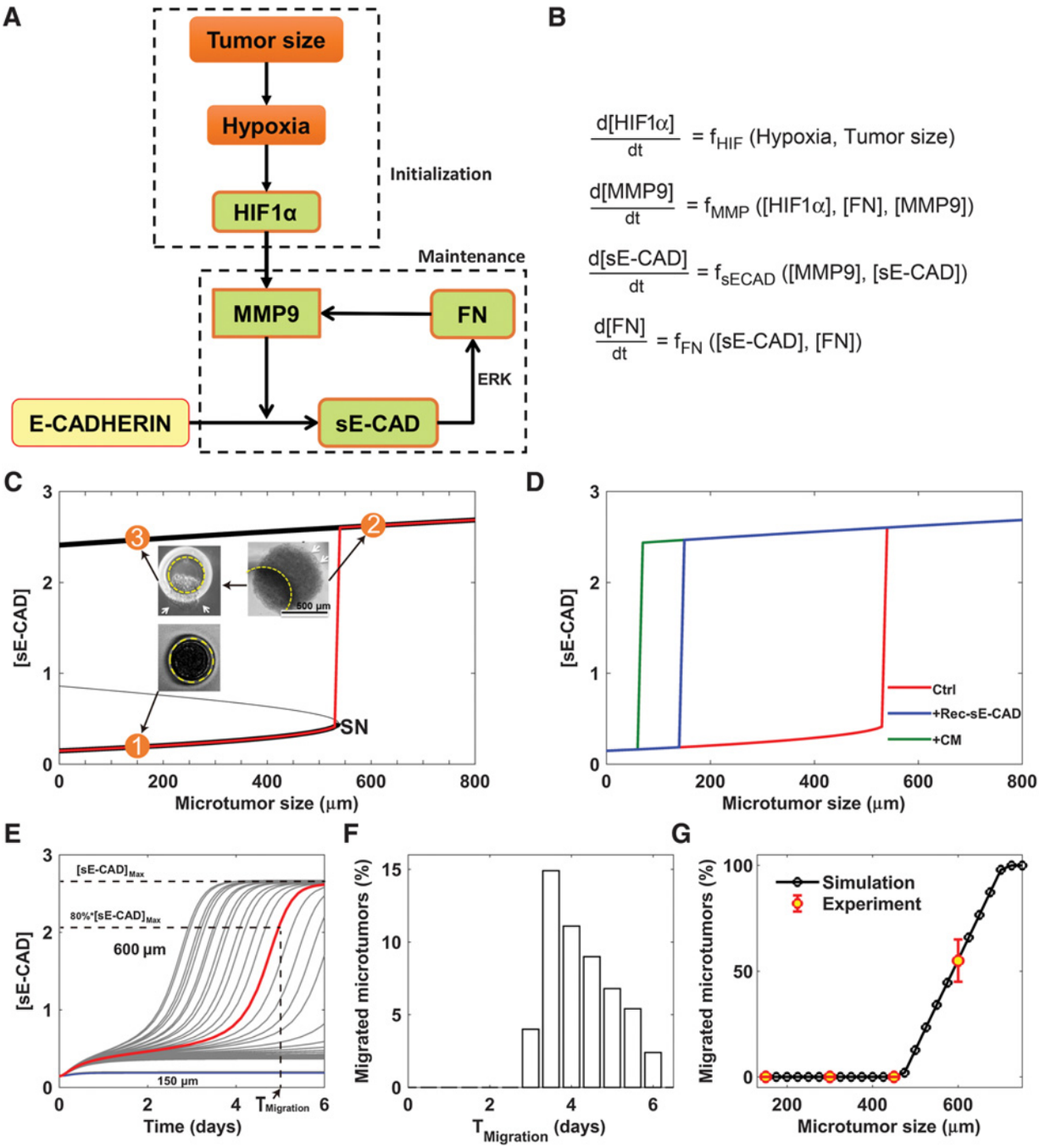

Figure 4.

Mathematical model predicts an irreversible bistable switch as the mechanism of the migratory behavior of the microtumor. **A,** Schematic depiction of the core regulatory network. **B,** The corresponding mathematical model described with ODE (details in the Supplementary Information). **C,** Bifurcation analysis of the mathematical model gives an irreversible bistable switch. There is a threshold (SN) of microtumor size for the activation of this switch. Case 1, 150 μm microtumor does not exceed the threshold and does not migrate. Case 2, Hypoxic microenvironment in 600 μm microtumor exceeds the threshold and induces high levels of [sE-CAD] and a migratory phenotype. Case 3, Regrowing 600 μm microtumors into nonhypoxic small microtumors still maintains high [sE-CAD] and migratory phenotype, suggesting irreversibility of the switch. **D,** The threshold of microtumor size for migration shifts to lower sizes (<200 μm) in the presence of Rec-sE-CAD (blue) or CM from migrated microtumor (green). **E,** The heterogeneous dynamics of the [sE-CAD] for 150 and 600 μm microtumors due to the intertumoral variation ($n = 30$ microtumors for each size). It is assumed that the microtumor migration becomes visible when [sE-CAD] exceeds 80% of its steady-state value with the corresponding time, $T_{migration}$. Unlike 600 μm microtumors, 150 μm microtumors have negligible variation. **F,** The distribution of $T_{migration}$ ($n = 1{,}000$ microtumors). **G,** Simulation and experimental data reveal that the percentage of the migrated microtumors depends on the microtumor size.

microtumors (Fig. 4G; ref. 25). To reproduce our experimental results, we assumed that microtumor migration becomes visible when sE-CAD exceeds 80% of its steady-state value with the corresponding time, $T_{migration}$ while the exact value of this threshold does not affect our conclusions in this work. The network in Fig. 4A suggests that one can inhibit microtumor migration by inhibiting regulators (HIF1α/MMPs/sE-CAD) while intertumoral variation may complicate the outcomes. We present our modeling and experimental studies in the next sections.

Antihypoxia treatment attenuates microtumor migration most effectively only when HIF1α is inhibited at early time points

On the basis of our two-stage progression mechanism, we hypothesized that inhibition of HIF1α is most effective during

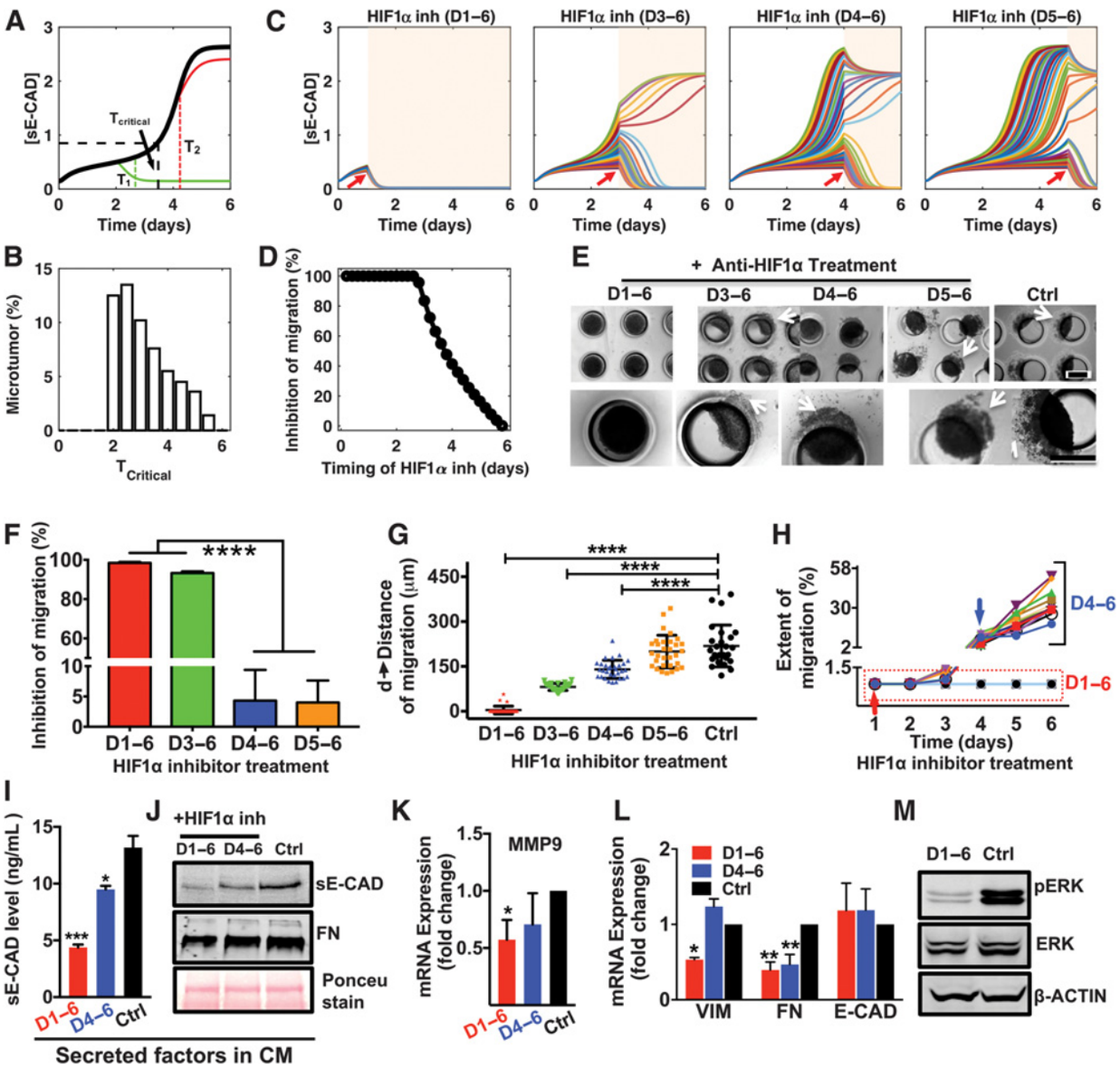

Figure 5.

HIF1α inhibition effectively attenuates microtumor migration only when HIF1α is inhibited at early time points. **A,** Mathematical model predicts a critical time ($T_{critical}$) to stop migration with HIF1α inhibition for single microtumor. HIF1α inhibition can attenuate microtumor migration (green) only if treated before the critical time (T1) but has no effect after the critical time (T2, red line). **B,** Distribution of $T_{critical}$ ($n = 1{,}000$ microtumors) emphasizes intertumoral variation. **C,** Dynamics of [sE-CAD] under HIF1α inhibition at different times ($n = 50$ microtumors for each case). Treatment periods shaded with light background. **D,** HIF1α inhibition started before day 3 inhibited microtumor migration significantly ($n = 1{,}000$ microtumors). **E,** Photomicrographs show migratory status of 600 μm microtumors on day 6 with HIF1α inhibition at different times. The effect of HIF1α inhibition on microtumor migration (**F**), distance of migration (**G**), and extent of migration (**H**). Each dot in **G** represents data for individual microtumor. Each line in **H** represents migration kinetics for individual microtumor, with HIF1α inhibition on day 1 (red arrow) or day 4 (blue arrow). HIF1α inhibition (D1–6) downregulated sE-CAD levels (ELISA; **I**), sE-CAD and FN expression (Western blot) in 600/CM (**J**), mRNA expression of MMP9 (**K**), VIM and FN (**L**), and protein expression of pERK (**M**). Data are presented as mean ± SEM. *, $P < 0.05$; **, $P < 0.01$; ****, $P < 0.0001$ with respect to untreated 600 μm microtumors; one-way ANOVA, followed by Tukey test.

the initialization stage. Figure 5A shows simulated time courses of [sE-CAD] without (black line) and with HIF1α inhibitor treatment of 600 μm microtumors at different times. The results show that a critical time exists (denoted as $T_{critical}$), where HIF1α inhibition starting from T_1 ($T_1<T_{critical}$) can effectively prevent increase in [sE-CAD] (green line), thus inhibiting microtumor migration. In contrast, HIF1α inhibition at T_2 ($T_2>T_{critical}$) cannot prevent further increase of already elevated [sE-CAD] (red line); hence the microtumor continues to migrate even in the presence of HIF1α inhibitor. This implies that there is a treatment window (0 to $T_{critical}$) for HIF1α inhibitor to be effective in restricting microtumor migration. Because of dynamic intertumoral variation, even microtumors of the same size have a distribution of $T_{critical}$ (Fig. 5B), which widens the boundary of this treatment window. Consequently, HIF1α inhibition is effective in inhibiting migration in most of the microtumors when started before $T_{criticial}$ while some microtumors still migrate when the treatment is started on day 3 ($T_{critical}<T<T_{migration}$). HIF1α inhibition from day 4 or day 5 ($T>T_{critical}$, $T_{migration}$) is not effective, showing migration in most of the microtumors (Fig. 5C and D). This implies that it is too late to stop migration with HIF1α inhibition when the bistable switch is turned on by the hypoxic microenvironment. Together, computational modeling strongly suggests that although the hypoxic microenvironment induces the migratory phenotype, HIF1α inhibition is effective only for a small time window of treatment and the window boundary is blurred by the existence of dynamic intertumoral variation.

To confirm our *in silico* results, we treated 600 μm microtumors with the chemical inhibitor of HIF1α starting on day 1 ($T<T_{critical}$, early inhibition), day 3 ($T_{critical}<T<T_{migration}$), day 4 or 5 ($T>T_{critical}$, $T_{migration}$, late inhibition) until day 6 of the culture. Interestingly, HIF1α inhibition from D1–6 or D3–6 inhibited microtumor migration significantly (only 3 and 11 of 290 microtumors showed migration; Fig. 5E–H). However, HIF1α inhibition after day 4 (D4–6, D5–6) did not block migration similar to the untreated large microtumors (Fig. 5E–H; Supplementary Fig. S6A and S6B). The distance and extent of migration showed tumor-to-tumor variation as evident by the distribution and the wider error bars (Fig. 5G) and this variation correlated with the delay in starting the HIF1α inhibitor treatment (Fig. 5G and H). Notably, these migratory microtumors continued to migrate even in presence of HIF1α inhibitor (Fig. 5H, blue arrow; Supplementary Fig. S6).

The HIF1α inhibition decreased [sE-CAD] from 13.1 ± 1.8 ng/mL (untreated controls) to 4.4 ± 0.4 ng/mL and 9.5 ± 0.5 ng/mL for D1–6 and D4–6 inhibition, respectively (Fig. 5I). Compared with the untreated microtumors, early (D1–6) HIF1α inhibition decreased [sE-CAD] and FN in the 600/CM (Fig. 5J) and significantly downregulated *MMP9* (Fig. 5K), *VIM*, and *FN* (Fig. 5L), without significant effect on *E-CAD* expression. Early HIF1α inhibition also reduced pERK expression significantly compared with untreated control (Fig. 5M; Supplementary Fig. S6C). Although D4–6 HIF1α inhibition reduced *FN* (both secreted in the CM and intracellular), this late inhibition could not reduce *MMP9* and *VIM* expression (Fig. 5K and L). These observations are consistent with and support our mathematical model reinforcing positive feedback loop between sE-CAD and MMP9 in the maintenance stage, and suggest that once established, such positive feedback may contribute to the ineffectiveness of HIF1α inhibition.

Together, these results suggest that early HIF1α inhibition ($T<T_{critical}$) can prevent microtumor migration while late inhibition ($T>T_{critical}$) does not work effectively. The results also support our hypothesis that hypoxia is important only for the initiation stage of microtumor migration and provide a mechanistic explanation for the clinical failure of antihypoxia treatments (18–20).

Blocking effects of sE-CAD by anti–sE-CAD antibody or preventing its shedding by MMP inhibitor effectively hinders microtumor migration

Our simulations predict that early ($T<T_{critical}$) sE-CAD inhibition will prevent/stop migration (Fig. 6A) by keeping [sE-CAD] low so that the bistable switch is not turned on to initiate the cascade necessary for microtumor migration. In the late inhibition ($T>T_{critical}$), although [sE-CAD] has exceeded the threshold causing some microtumors to migrate, sE-CAD inhibition turns the bistable switch off, and these microtumors cease to migrate further (Fig. 6A and B). That is, although fraction of migrated microtumor increases with the time of anti–sE-CAD treatment [Fig. 6B(i)], the fraction of continuously migrating microtumor disappears independent of time of anti–sE-CAD treatment [Fig. 6B(ii)]. We obtained similar simulation results by inhibiting MMP-mediated sE-CAD shedding (Supplementary Fig. S7A and S7B). Together, these computational results suggest that unlike HIF1α inhibition, the effectiveness of sE-CAD or MMP inhibition is independent of time of treatment and intertumoral variation.

To experimentally test the above model predictions, we blocked effects of sE-CAD in 600 μm microtumors using antibody against the extracellular domain of E-CAD (H-108, Santa Cruz Biotechnology, 40 μg/mL). Anti–sE-CAD antibody treatment scavenged the cleaved sE-CAD and reduced the secreted FN in the CM compared with the untreated control (Fig. 6C and D). Anti–sE-CAD treatment on D3–6 completely inhibited collective migration (Supplementary Fig. S8A, left). Although few microtumors treated with anti–sE-CAD antibody on D4–6 exhibited some migration (that was started before the treatment), the distance and extent of migration was significantly lower (38.4 ± 6.5 μm and <25%, respectively; Fig. 6E and F) compared with that achieved with HIF1α inhibition on D4–6 (145.4 ± 25.3 μm and 26%–50%, respectively; Fig. 5G and H). Indeed, the single microtumor trajectories clearly show that these already migrated microtumors stopped migration after anti–sE-CAD antibody treatment (Fig. 6F, blue arrow). The tight distribution of distance and extent of migration (Fig. 6E and F) also confirms our mathematical predictions that all treated microtumors respond similarly with minimal effect of intertumoral variation. These findings were further confirmed by qRT-PCR showing significant downregulation of *MMP9* (Fig. 6G) and *FN* (Fig. 6H) with no significant change in *VIM* and *E-CAD* after anti–sE-CAD antibody treatments. We observed similar results in primary mBC microtumors where anti–sE-CAD antibody treatment (D4–7) limited microtumor migration (Supplementary Fig. S8B), downregulated *MMP9* expression (Supplementary Fig. S8C) without altering mesenchymal marker expression (Supplementary Fig. S8D), and decreased sE-CAD levels (Supplementary Fig. S8E). This could be due to already elevated mesenchymal marker expression in mBC cells derived from metastatic tumors (Supplementary Fig. S3).

In addition, we blocked sE-CAD shedding in 600 μm microtumors by broad MMP inhibitor, GM6001 (20 μmol/L) on day 1

($T<T_{critical}$) or day 4 ($T>T_{critical}$). MMP inhibition reduced sE-CAD shedding and secreted FN levels in the CM at both treatment times (Fig. 7A and B). *MMP9* mRNA expression was significantly downregulated at both treatment time points (Fig. 7C). We observed no migration for MMP inhibition started on day 1 whereas D4–6 treatment completely ceased the migration (Fig. 7D; Supplementary Fig. S7C). Early MMP inhibition ($T<T_{critical}$, D1–6) downregulated *VIM* and *FN* expression significantly without significant effect on *E-CAD* compared with untreated microtumors (Fig. 7E). On the other hand, late MMP inhibition ($T>T_{critical}$, D4–6)

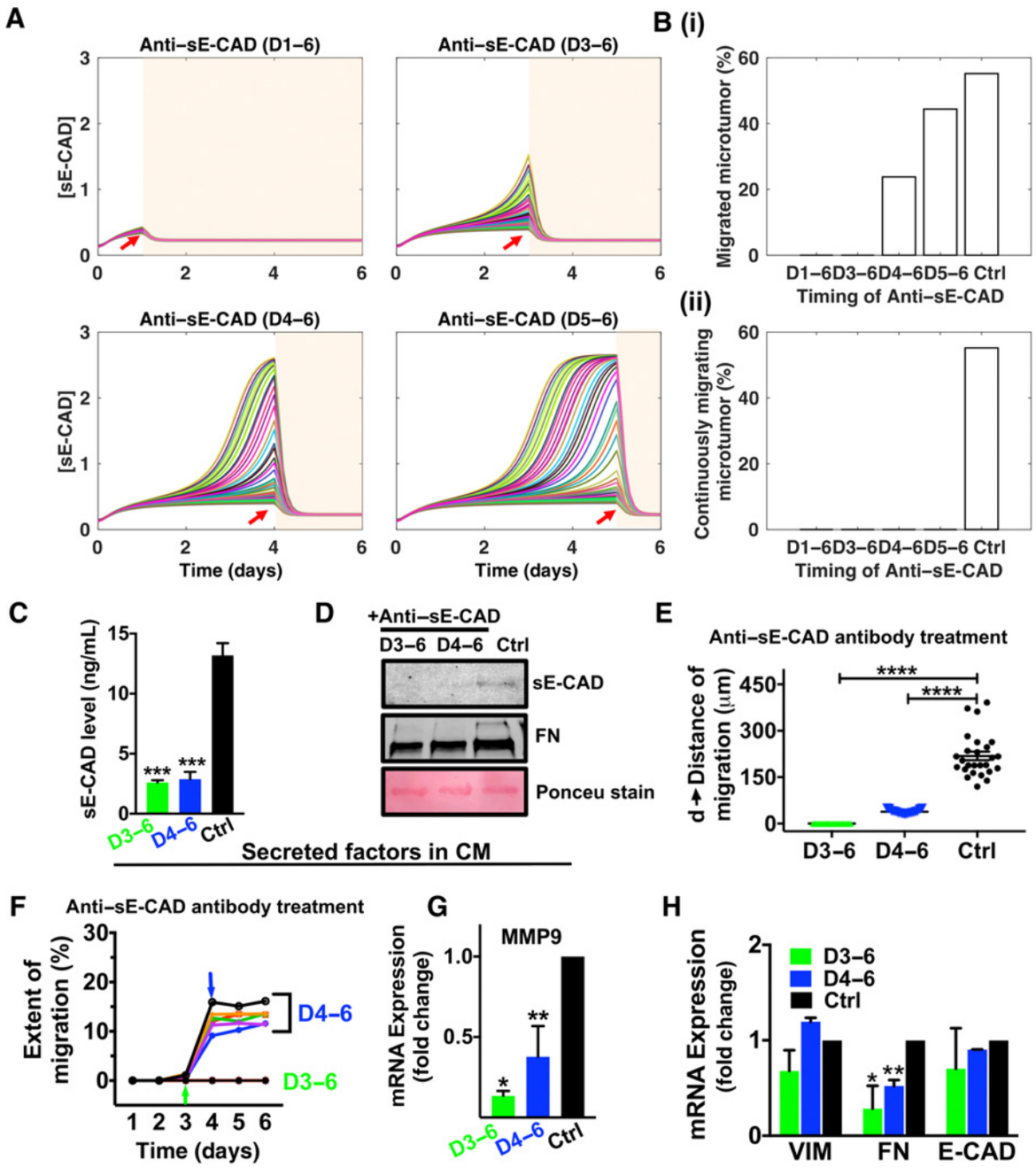

Figure 6.

Inhibition of sE-CAD by anti–E-CAD antibody attenuated collective migration in 600 μm microtumors. **A,** The dynamics of [sE-CAD] in 50 microtumors post anti–sE-CAD antibody treatment started on day 1, day 3, day 4, and day 5 (red arrows). **B,** The fraction of migrated microtumors (top; **i**) and continuously migrating microtumors (bottom; **ii**) with anti–sE-CAD antibody treatment ($n = 1{,}000$ microtumors). Anti–sE-CAD antibody treatment (40 μg/mL) on day 3 and day 4 reduced sE-CAD levels (ELISA; **C**), reduced sE-CAD and FN expression (Western blot) in 600/CM (**D**), reduced distance of migration (**E**), reduced extent of migration (**F**), and downregulated mRNA expression of MMP9 (**G**) and FN (**H**). Data are drawn from three independent experiments and are presented as means ± SEM. *, $P < 0.05$; **, $P < 0.01$, ***, $P < 0.001$; ****, $P < 0.0001$ with respect to untreated control; one-way ANOVA, followed by Tukey test.

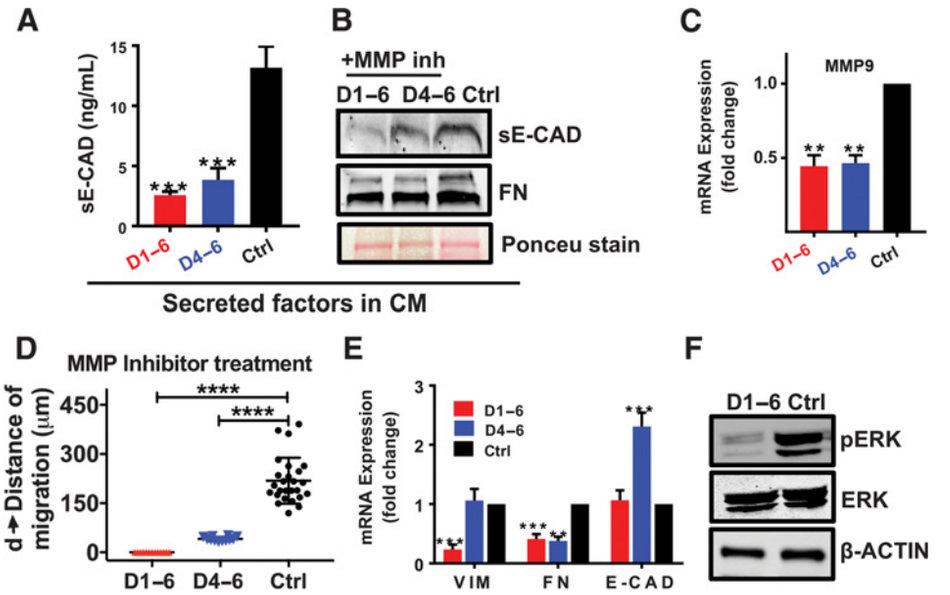

Figure 7.
MMP inhibitor treatment attenuated collective migration in a time-independent manner. MMP inhibitor treatment (20 μmol/L of GM6001) on days 1–6 and days 4–6 decreased sE-CAD levels (ELISA; **A**), decreased sE-CAD and FN expression (Western blot) in 600/CM (**B**), downregulated MMP9 mRNA expression (**C**), inhibited migration significantly (**D**), downregulated VIM and FN mRNA expression (**E**), and downregulated pERK microtumors compared with untreated controls (**F**). Data are presented as means ± SEM from three independent experiments. **, $P < 0.01$; ***, $P < 0.001$; ****, $P < 0.0001$; one-way ANOVA, followed by Tukey test. w.r.t., untreated control.

downregulated *FN* expression significantly without altering *VIM* expression similar to anti–sE-CAD treatment. MMP inhibition also reduced pERK/ERK ratio and ERK activation (Fig. 7F; Supplementary Fig. S7D). Notably, *VIM* expression was downregulated only with early inhibition of HIF1α and MMPs in the initialization stage while it had no effect when these molecules were inhibited in the maintenance stage. MMP inhibition (D4–7) prevented migration in primary mBC microtumors (Supplementary Fig. S7E) and downregulated *MMP9* and *FN* expression along with decreased sE-CAD levels compared with untreated control (Supplementary Fig. S7F–S7H).

Together, experimental results in T47D and multiple primary patient-derived microtumors confirmed the predictions from our mathematical model. MMPs, sE-CAD, and FN are the components of the positive feedback loop and are critical to the irreversible bistable switch, and to maintain the microtumor migration. HIF1α, on the other hand, is a major trigger of the switch, which is dispensable once the switch is turned on. These results confirmed our two-stage progression model that HIF1α is important only in the initialization stage of tumor progression. Consequently, inhibiting HIF1α is only effective before $T_{critical}$, which varies from tumor to tumor. Once MMPs, sE-CAD, and FN accumulate and exceed threshold values, targeting these molecules is more effective in inhibiting microtumor migration, and has less constraints of the treatment time and dynamic tumor intertumoral variation.

Discussion

Solid tumor growth generates multiple layers of cells that build a physical barrier to diffusion of oxygen, nutrients and metabolites, leading to hypoxic tumor microenvironment, which further drives aggressive phenotype due to activation of various downstream signaling pathways (2, 11, 13). Hypoxic microenvironment further induces secretome, which contains many secreted factors, sheddases, and proteases that reshape the tumor microenvironment, modulate cellular phenotypes, and affect drug responses (2, 5, 6, 47). For in-depth mechanistic understanding of role of hypoxia and hypoxic secretome in inducing migratory phenotypes, it is desirable to have an experimental system that recapitulates spontaneously formed hypoxic microenvironment along with the tumor secretome because traditional 2D cell culture–based systems are unable to capture constantly evolving dynamic microenvironment (13).

To address this challenge, we engineered 3D microtumor models with controlled microenvironments to investigate the intricate core regulatory network implicated in inducing migration. We observed microtumor size–induced hypoxic signaling that leads to upregulation of mesenchymal markers and collective migration without loss of epithelial cadherin in large microtumors (25). The observed high levels of HIF1α, MMPs, sE-CAD, and FN in large microtumors suggest the interplay between hypoxia and hypoxic secretome for maintaining the migratory phenotype. Clinical data extracted from 3,735 human breast tumor samples revealed higher levels of FN and MMP9 compared with normal mammary gland corroborating our findings. Through theoretical analysis with a minimal mathematical model, we proposed an irreversible bistable switch mechanism by which tumor cells migrate collectively once the microtumor grows larger than a preset threshold size. Our computational model successfully explained experimentally observed irreversible nature of the migratory phenotype in large microtumors and also predicted the efficacy of temporal inhibition of HIF1α, MMPs, and sE-CAD in halting microtumor migration. Different molecular species play temporally different roles in tumor progression, and proper choice of drug targets can minimize negative effects of such constantly evolving microenvironments on treatment efficacy (21, 48). Indeed, through computational and experimental approaches, we predicted and validated a novel mechanism of two-stage tumor progression where hypoxia is critical in initiating the migratory phenotype, which is then maintained by tumor-secreted factors such as MMPs, sE-CAD, and FN. We acknowledge that the proposed mathematical model of regulatory network is

far from complete to characterize all the changes required for induction of tumor migration. The transcriptomic and proteomic profiles of these complementary 3D models (hypoxic and migratory large microtumors, nonhypoxic nonmigratory small microtumors, and hypoxic CM-treated nonhypoxic yet migratory small microtumors) will provide more complete mechanistic insights in our future study.

Because the hypoxia-induced HIF1α plays an important role only at the initial stage of activating the bistable switch, HIF1α inhibition can effectively halt tumor migration only if treated prior to the onset of migratory phenotypes ($T<T_{migration}$), which is not easy in practice due to the stochastic dynamics of tumor growth. This further explains failure of HIF1α inhibition strategies to stop tumor progression in clinics, as it may be too late to stop the entire signaling cascade induced by HIF1α in already hypoxic tumors. Both our computational and experimental studies demonstrate that efficacy of HIF1α inhibition to prevent tumor migration is significantly affected by treatment initiation time and intertumoral variation, leading to variable treatment efficacy, consistent with the conflicting results observed in the clinical studies (18–20).

Our mathematical prediction of two-stage progression mechanism suggests that the sE-CAD/MMP/FN axis mainly functions to maintain the migratory phenotype, and its inhibition is less affected by the stochastic tumor growth. Experimentally, inhibition of sE-CAD by MMP inhibitor or by anti–E-CAD antibody, both suppressed the collective migration in T47D and primary patient-derived microtumors. Unlike HIF1α inhibition, sE-CAD inhibition was much less affected by intertumoral variation. We propose sE-CAD as a potential target because it seems not to have an essential physiologic role (49), pharmaceutical intervention to keep sE-CAD below a threshold level may not increase toxicity of concurrent antineoplastic regimens. Furthermore, unlike the treatment strategies targeting inhibition of tumor growth, the strategy proposed here of targeting tumor-secreted factors to constrain tumor migration may impose much less selection pressure as predicted from cancer evolutionary theory (50).

Another important aspect of this study is our ability to cross-examine roles of different regulators such as pharmacologic inhibition in hypoxic, migratory large microtumors and stimulation/induction in nonhypoxic, nonmigratory small microtumors, using complementary, yet controlled model systems made of the same parent cells. For instance, inhibition of sE-CAD by anti–E-CAD antibody stops migration in large hypoxic microtumors by downregulating *FN*, but without affecting *VIM* expression. Also, stimulation with human Rec-sE-CAD induces collective migration and *FN* upregulation in nonhypoxic, nonmigratory small microtumors without affecting *VIM* expression, suggesting that sE-CAD is not an effective regulator of *VIM*, and *VIM* is dispensable for migration. The role of epithelial and mesenchymal phenotypes in cancer cell migration has been widely debated in recent years (3, 51, 52). Our results suggest coexistence of multiple distinct phenotypes as indicated by differential expression patterns of *VIM* and *FN*, and these phenotypes cannot be sufficiently characterized by individual mesenchymal marker as in the two controversial studies (51, 52). Further studies are needed to examine whether these phenotypes actively contribute to migration or are simply passive outcomes of the microenvironment.

In summary, our combined experimental and mathematical modeling studies demonstrate the importance of taking into account the temporal dynamics of evolving tumor microenvironments, resonant with other studies stressing dynamic pharmacology (53). We provide insight into how HIF1α, MMP, E-CAD, and FN work together to generate emergent properties, more specifically, the irreversibility of the migratory phenotype, and provide evidence that it is more effective and practical to target network components (e.g., sE-CAD) that control the migratory phenotype maintenance instead of those (e.g., HIF1α) for the initialization stage. While in this article, we focused on a few tumor-secreted factors, both our experimental system and computational approach can be readily applied to include couplings between the secretome network and intracellular signal transduction and gene regulation networks. The microtumor models can uniquely provide quantitative information of the temporal evolution of both, the microenvironment and cell phenotypes in an approachable experimental setting, and identify combined therapeutic strategies that overcome problems of drug resistance of existing ones (21, 47).

Disclosure of Potential Conflicts of Interest

No potential conflicts of interest were disclosed.

Authors' Contributions

Conception and design: X.-J. Tian, V.S. Donnenberg, A.M. Watson, J. Xing, S. Sant

Development of methodology: M. Singh, X.-J. Tian, V.S. Donnenberg, A.M. Watson, J. Xing, S. Sant

Acquisition of data (provided animals, acquired and managed patients, provided facilities, etc.): M. Singh, X.-J. Tian, V.S. Donnenberg, A.M. Watson, L.P. Stabile, S.C. Watkins, S. Sant

Analysis and interpretation of data (e.g., statistical analysis, biostatistics, computational analysis): M. Singh, X.-J. Tian, V.S. Donnenberg, A.M. Watson, J. Zhang, J. Xing, S. Sant

Writing, review, and/or revision of the manuscript: M. Singh, X.-J. Tian, V.S. Donnenberg, A.M. Watson, L.P. Stabile, J. Xing, S. Sant

Administrative, technical, or material support (i.e., reporting or organizing data, constructing databases): X.-J. Tian, J. Xing, S. Sant

Study supervision: V.S. Donnenberg, J. Xing, S. Sant

Acknowledgments

We thank Dr. Wen Xie, University of Pittsburgh School of Pharmacy, for providing access to the core facilities. We thank Drs. Barry Gold and Vinayak Sant, Department of Pharmaceutical Sciences, University of Pittsburgh School of Pharmacy, for critical reading and insightful suggestions on the manuscript. This work is supported by the Department of Pharmaceutical Sciences, School of Pharmacy University of Pittsburgh (SS), NIH (grant no. R37CA232209 to S. Sant, J. Xing, V.S. Donnenberg, S.C. Watkins); the National Science Foundation (grant no. DMS-1462049 to J. Xing); the Pennsylvania Department of Health (grant no. SAP 4100062224 to J. Xing); BC032981, BC044784, W81XWH-12-1-0415, and BC132245_W81XWH-14-0258 from the Department of Defense (to V.S. Donnenberg); the Hillman Foundation (to V.S. Donnenberg); and the Glimmer of Hope Foundation (to V.S. Donnenberg). The confocal microscope in the Center for Biologic Imaging at University of Pittsburgh is UPCI supported by 1S10OD019973-01 (to S.C. Watkins). Cytometry Facility is supported by CCSG P30CA047904.

The costs of publication of this article were defrayed in part by the payment of page charges. This article must therefore be hereby marked *advertisement* in accordance with 18 U.S.C. Section 1734 solely to indicate this fact.

Received October 16, 2018; revised February 1, 2019; accepted March 29, 2019; published first April 5, 2019.

References

1. Gilkes DM, Semenza GL, Wirtz D. Hypoxia and the extracellular matrix: drivers of tumour metastasis. Nat Rev Cancer 2014;14:430–9.
2. Rankin EB, Giaccia AJ. Hypoxic control of metastasis. Science 2016;352: 175–80.
3. Nieto MA, Huang RY, Jackson RA, Thiery JP. EMT: 2016. Cell 2016;166: 21–45.
4. Cheung KJ, Ewald AJ. Illuminating breast cancer invasion: diverse roles for cell-cell interactions. Curr Opin Cell Biol 2014;30:99–111.
5. Miller MA, Oudin MJ, Sullivan RJ, Wang SJ, Meyer AS, Im H, et al. Reduced proteolytic shedding of receptor tyrosine kinases is a post-translational mechanism of kinase inhibitor resistance. Cancer Discov 2016;6:382–99.
6. Karagiannis GS, Pavlou MP, Diamandis EP. Cancer secretomics reveal pathophysiological pathways in cancer molecular oncology. Mol Oncol 2010;4:496–510.
7. Cox TR, Rumney RMH, Schoof EM, Perryman L, Hoye AM, Agrawal A, et al. The hypoxic cancer secretome induces pre-metastatic bone lesions through lysyl oxidase. Nature 2015;522:106–10.
8. Brouxhon SM, Kyrkanides S, Teng X, Raja V, O'Banion MK, Clarke R, et al. Monoclonal antibody against the ectodomain of E-cadherin (DECMA-1) suppresses breast carcinogenesis: involvement of the HER/PI3K/Akt/mTOR and IAP pathways. Clin Cancer Res 2013;19: 3234–46.
9. Overall CM, Lopez-Otin C. Strategies for MMP inhibition in cancer: innovations for the post-trial era. Nat Rev Cancer 2002; 2:657–72.
10. Paltridge JL, Belle L, Khew-Goodall Y. The secretome in cancer progression. Biochim Biophys Acta 2013;1834:2233–41.
11. Kao SH, Wu KJ, Lee WH. Hypoxia, epithelial-mesenchymal transition, and TET-mediated epigenetic changes. J Clin Med 2016;5. doi: 10.3390/jcm5020024.
12. Grigore AD, Jolly MK, Jia D, Farach-Carson MC, Levine H. Tumor budding: the name is EMT. Partial EMT. J Clin Med 2016;5. doi: 10.3390/jcm5050051.
13. Nobre AR, Entenberg D, Wang Y, Condeelis J, Aguirre-Ghiso JA. The different routes to metastasis via hypoxia-regulated programs. Trends Cell Biol 2018;28:941–56.
14. Tian XJ, Zhang H, Xing J. Coupled reversible and irreversible bistable switches underlying TGFbeta-induced epithelial to mesenchymal transition. Biophys J 2013;105:1079–89.
15. Zhang J, Tian XJ, Zhang H, Teng Y, Li R, Bai F, et al. TGF-beta-induced epithelial-to-mesenchymal transition proceeds through stepwise activation of multiple feedback loops. Sci Signal 2014;7:ra91.
16. Young SD, Marshall RS, Hill RP. Hypoxia induces DNA overreplication and enhances metastatic potential of murine tumor cells. Proc Natl Acad Sci U S A 1988;85:9533–7.
17. Young SD, Hill RP. Effects of reoxygenation on cells from hypoxic regions of solid tumors: anticancer drug sensitivity and metastatic potential. J Natl Cancer Inst 1990;82:371–80.
18. Mack PC, Redman MW, Chansky K, Williamson SK, Farneth NC, Lara PN, et al. Lower osteopontin plasma levels are associated with superior outcomes in advanced non-small-cell lung cancer patients receiving platinum-based chemotherapy: SWOG Study S0003. J Clin Oncol 2008; 26:4771–6.
19. Patel A, Sant S. Hypoxic tumor microenvironment: opportunities to develop targeted therapies. Biotechnol Adv 2016;34:803–12.
20. Williamson SK, Crowley JJ, Lara PN, McCoy J, Lau DHM, Tucker RW, et al. Phase III trial of paclitaxel plus carboplatin with or without tirapazamine in advanced non–small-cell lung cancer: Southwest Oncology Group Trial S0003. J Clin Oncol 2005;23:9097–104.
21. Donnenberg VS, Donnenberg AD. Stem cell state and the epithelial-to-mesenchymal transition: implications for cancer therapy. J Clin Pharmacol 2015;55:603–19.
22. Gong X, Lin C, Cheng J, Su J, Zhao H, Liu T, et al. Generation of multicellular tumor spheroids with microwell-based agarose scaffolds for drug testing. PLoS One 2015;10:e0130348.
23. Nyberg SL, Hardin J, Amiot B, Argikar UA, Remmel RP, Rinaldo P. Rapid, large-scale formation of porcine hepatocyte spheroids in a novel spheroid reservoir bioartificial liver. Liver Transpl 2005;11: 901–10.
24. Sant S, Johnston PA. The production of 3D tumor spheroids for cancer drug discovery. Drug Discov Today Technol 2017;23:27–36.
25. Singh M, Mukundan S, Jaramillo M, Oesterreich S, Sant S. Three-dimensional breast cancer models mimic hallmarks of size-induced tumor progression. Cancer Res 2016;76:3732–43.
26. Singh M, Close DA, Mukundan S, Johnston PA, Sant S. Production of uniform 3D microtumors in hydrogel microwell arrays for measurement of viability, morphology, and signaling pathway activation. Assay Drug Dev Technol 2015;13:570–83.
27. Singh M, Warita K, Warita T, Faeder JR, Lee REC, Sant S, et al. Shift from stochastic to spatially-ordered expression of serine-glycine synthesis enzymes in 3D microtumors. Sci Rep 2018;8:9388.
28. Singh M, Venkata Krishnan H, Ranganathan S, Kiesel B, Beumer JH, Sreekumar S, et al. Controlled three-dimensional tumor microenvironments recapitulate phenotypic features and differential drug response in early vs. advanced stage breast cancer. ACS Biomater Sci Eng 2018;4: 421–31.
29. Donnenberg VS, Donnenberg AD, Zimmerlin L, Landreneau RJ, Bhargava R, Wetzel RA, et al. Localization of CD44 and CD90 positive cells to the invasive front of breast tumors. Cytometry B Clin Cytom 2010;78: 287–301.
30. Donnenberg VS, Landreneau RJ, Pfeifer ME, Donnenberg AD. Flow cytometric determination of stem/progenitor content in epithelial tissues: an example from nonsmall lung cancer and normal lung. Cytometry A 2013; 83:141–9.
31. Susaki EA, Tainaka K, Perrin D, Kishino F, Tawara T, Watanabe TM, et al. Whole-brain imaging with single-cell resolution using chemical cocktails and computational analysis. Cell 2014;157:726–39.
32. Watson AM, Rose AH, Gibson GA, Gardner CL, Sun C, Reed DS, et al. Ribbon scanning confocal for high-speed high-resolution volume imaging of brain. PLoS One 2017;12:e0180486.
33. Frankowski H, Gu YH, Heo JH, Milner R, Del Zoppo GJ. Use of gel zymography to examine matrix metalloproteinase (gelatinase) expression in brain tissue or in primary glial cultures. Methods Mol Biol 2012;814: 221–33.
34. Espina V, Liotta LA. What is the malignant nature of human ductal carcinoma in situ? Nat Rev Cancer 2011;11:68–75.
35. De Sousa EMF, Vermeulen L, Fessler E, Medema JP. Cancer heterogeneity–a multifaceted view. EMBO Rep 2013;14:686–95.
36. Khalil AA, Ilina O, Gritsenko PG, Bult P, Span PN, Friedl P. Collective invasion in ductal and lobular breast cancer associates with distant metastasis. Clin Exp Metastasis 2017;34:421–9.
37. Choi JY, Jang YS, Min SY, Song JY. Overexpression of MMP-9 and HIF-1alpha in breast cancer cells under hypoxic conditions. J Breast Cancer 2011;14:88–95.
38. Chua YL, Dufour E, Dassa EP, Rustin P, Jacobs HT, Taylor CT, et al. Stabilization of hypoxia-inducible factor-1alpha protein in hypoxia occurs independently of mitochondrial reactive oxygen species production. J Biol Chem 2010;285:31277–84.
39. Brouxhon SM, Kyrkanides S, Teng X, Athar M, Ghazizadeh S, Simon M, et al. Soluble E-cadherin: a critical oncogene modulating receptor tyrosine kinases, MAPK and PI3K/Akt/mTOR signaling. Oncogene 2014;33:225–35.
40. David JM, Rajasekaran AK. Dishonorable discharge: the oncogenic roles of cleaved E-cadherin fragments. Cancer Res 2012;72:2917–23.
41. Repetto O, De Paoli P, De Re V, Canzonieri V, Cannizzaro R. Levels of soluble E-cadherin in breast, gastric, and colorectal cancers. BioMed Res Int 2014;2014:408047.
42. Najy AJ, Day KC, Day ML. The ectodomain shedding of E-cadherin by ADAM15 supports ErbB receptor activation. J Biol Chem 2008;283: 18393–401.
43. Inge LJ, Barwe SP, D'Ambrosio J, Gopal J, Lu K, Ryazantsev S, et al. Soluble E-cadherin promotes cell survival by activating epidermal growth factor receptor. Exp Cell Res 2011;317:838–48.
44. Brouxhon SM, Kyrkanides S, Teng X, O'Banion MK, Clarke R, Byers S, et al. Soluble-E-cadherin activates HER and IAP family members in HER2+ and TNBC human breast cancers. Mol Carcinog 2014;53:893–906.
45. Grabowska MM, Sandhu B, Day ML. EGF promotes the shedding of soluble E-cadherin in an ADAM10-dependent manner in prostate epithelial cells. Cell Signal 2012;24:532–8.

46. Moshal KS, Sen U, Tyagi N, Henderson B, Steed M, Ovechkin AV, et al. Regulation of homocysteine-induced MMP-9 by ERK1/2 pathway. Am J Physiol Cell Physiol 2006;290:C883–91.
47. Miller MA, Sullivan RJ, Lauffenburger DA. Molecular pathways: receptor ectodomain shedding in treatment, resistance, and monitoring of cancer. Clin Cancer Res 2017;23:623–9.
48. Schmidt KT, Chau CH, Price DK, Figg WD. Precision oncology medicine: the clinical relevance of patient-specific biomarkers used to optimize cancer treatment. J Clin Pharmacol 2016;56:1484–99.
49. Grabowska MM, Day ML. Soluble E-cadherin: more than a symptom of disease. Front Biosci 2012;17:1948–64.
50. Greaves M, Maley CC. Clonal evolution in cancer. Nature 2012;481: 306–13.
51. Zheng X, Carstens JL, Kim J, Scheible M, Kaye J, Sugimoto H, et al. Epithelial-to-mesenchymal transition is dispensable for metastasis but induces chemoresistance in pancreatic cancer. Nature 2015;527: 525–30.
52. Fischer KR, Durrans A, Lee S, Sheng J, Li F, Wong STC, et al. Epithelial-to-mesenchymal transition is not required for lung metastasis but contributes to chemoresistance. Nature 2015;527:472–6.
53. Behar M, Barken D, Werner SL, Hoffmann A. The dynamics of signaling as a pharmacological target. Cell 2013;155:448–61.